

Anion Redistribution in Solvation Structure Enables a Stable Graphite Cathode in Dual-Ion Batteries

Xin Hu, Wen Sun, Anbin Zhou, Ziyue Wen, Huirong Wang, Zhengqiang Hu, Tianyang Xue, Yongxin Huang,* Li Li, Feng Wu, and Renjie Chen*



Cite This: *ACS Nano* 2025, 19, 18686–18697



Read Online

ACCESS |

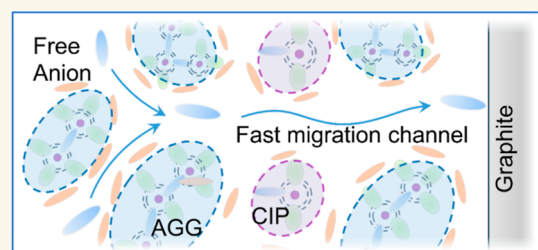
Metrics & More

Article Recommendations

Supporting Information

ABSTRACT: The electrochemical properties of anions as carriers in graphite-based dual-ion batteries (GDIBs) play an important role in achieving long cycling stability and high-rate performance. However, anion behavior in the electrolyte was neglected in previous studies. To balance high voltage and fast conduction, the anion behavior after introducing diluent in a highly concentrated electrolyte (HCE) to form locally highly concentrated electrolyte (LHCE) in GDIBs was deeply investigated. In contrast to the highly aggregated coordinated ion pairs in the HCE, more free anions can be attained in the LHCE without significant reunion. These free anions can rapidly migrate to the electrode surface under the electric field drive and then intercalate between graphite layers with a lower energy barrier. Meanwhile, an inorganic-rich interfacial layer with rapid ion conduction and a thinner thickness can be formed to prevent further decomposition of anions and stabilize the structure of the cathode. As a consequence, the dual-graphite DIBs achieved a superior capacity of 98.3% after 1000 cycles at a high rate of 200 mA g^{-1} in LHCE, and the corresponding pouch cells exhibited a stable cycling process. This work advances the understanding of anion chemistry, enabling the regulation of the anion status to enhance the electrochemical performance of GDIBs.

KEYWORDS: anion chemistry, anion redistribution, GDIBs, electrolyte, interfacial layer



INTRODUCTION

The rapid growth of energy consumption has driven the fast development of clean energy and reliable energy storage technology, which can achieve the function of peak-shaving and valley-filling for the power system.^{1,2} Currently, lithium-ion batteries and sodium-ion batteries have attracted major attention to large-scale energy storage.³ To meet more application scenarios, various electrochemical energy storage technologies are still widely developed to achieve a balance between cost, performance, resources, and manufacturing.⁴ Therefore, graphite-based dual-ion batteries (GDIBs) with low cost, good safety, and high voltage are emerging as promising candidates for large-scale energy storage.^{5–7}

Since 1938, Rudöf reported the intercalation of HSO_4^- into graphite; recently, the GDIBs were proposed as a new energy storage approach in 2012.⁸ On the one hand, the specific capacity of GDIBs is restricted by the intercalation reaction of anions with large size and high molar mass, such as ClO_4^- , HSO_4^{2-} , PF_6^- , FSI^- , and TFSI^- .^{9,10} On the other hand, due to the high embedded energy barrier of anions into the cathodic graphite, GDIBs exhibit a high operating voltage

plateau between 4.5 and 5.3 V, corresponding to an excellent discharging energy density.^{9,11} However, high operating voltage may introduce significant complexities to the electrochemical reaction, for instance, the instability of electrolytes and incompatibility of cathodes. In the final analysis, anion chemistry plays an important role in high-performance GDIBs.¹² Within the high voltage range, anions tend to decompose at the cathode surface, leading to the formation of the cathodic electrolyte interphase (CEI) layer. Since anions act as carriers involved in the intercalation process, the depletion of anions signifies a deterioration in electrochemical performance due to the limited active intercalation and deintercalation processes.¹³ Moreover, anions confined in the lithium ion (Li^+) solvation structure reduce the oxidative

Received: February 20, 2025

Revised: April 24, 2025

Accepted: April 28, 2025

Published: May 7, 2025



ACS Publications

© 2025 American Chemical Society

18686

<https://doi.org/10.1021/acsnano.5c03112>
ACS Nano 2025, 19, 18686–18697

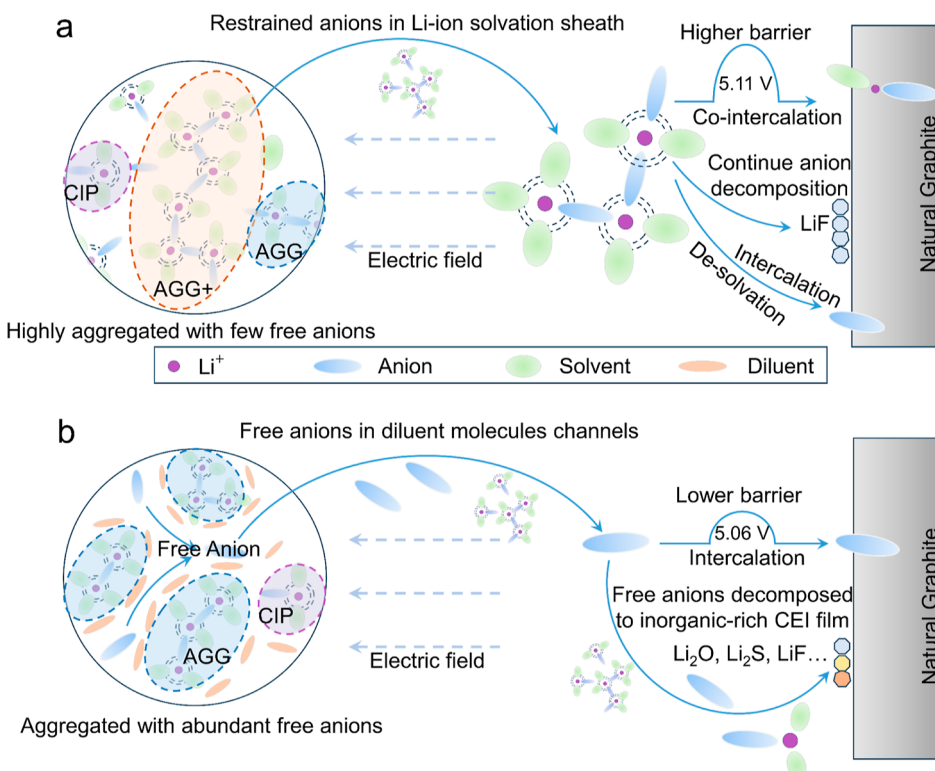


Figure 1. Schematic showing different behaviors of the anion in different electrolytes. (a) Illustration of highly aggregated ion pairs with few free anions and anion behaviors in HCE. (b) Illustration of aggregated ion pairs with abundant free anions and anion behaviors in locally highly concentrated electrolyte (LHCE).

stability of the electrolyte and exacerbate the fragmentation of the graphite electrode under solvent intercalation.^{14–16} To address the issues of interface degradation, anion consumption, and solvent cointercalation, a lot of works focuses on the anion chemistry in GDIBs, involving specific means of electrolyte design, interface construction, and anionic additives.^{17–22} As key factors in electrolyte design, composition and concentration may affect the quantity, intercalation kinetics, and interface evolution of cations and anions during the long cycling.^{22–24} Hence, highly concentrated electrolyte (HCE) has been developed to attain sufficient ions and a wide electrochemical window for GDIBs.^{5,25} However, the high viscosity and high cost of HCE result in slow kinetics and difficult application. Besides, more highly aggregated coordinated ion pair (AGG+) can be detected in HCE, leading to cointercalation of solvent and continued consumption of anions (Figure 1a).²⁶

In brief, the solvation structure of cations and anions should be adjusted to achieve low desolvation energy, a stable interface, and a viable intercalation energy barrier, which can be regarded as rate-determining steps for highly efficient GDIBs. Therefore, we introduce an LHCE to redistribute anions in the electrolyte. We select the 1,1,2,2-tetrafluoroethyl-2,2,3,3-tetrafluoropropyl ether (TTE) as a diluent in tetramethylene sulfone (TMS, which is stable under high voltage) solvent due to its several advantages, including low viscosity, high ignition point, and great infiltration. Besides, TTE is able to inhibit the dendrite growth of the alkaline metal anode and improve the Columbic efficiency of batteries.^{27,28} To investigate the anion behavior in LHCE, a LiFSI-3TMS-3TTE (where the numbers mean ratio in molar) electrolyte was adopted to GDIBs. In contrast, low-concentrated electro-

lyte (LCE) with solvent-separated ion pairs and HCE with contact ion pairs (CIPs) and aggregates (AGGs) were employed as a contrast sample.^{21,29,30} Compared with HCE (LiFSI-3TMS) and LCE (LiFSI-8TMS), the LHCE can attain both antioxidant properties and low viscosity, which is conducive to the stability and reaction kinetics of GDIBs.³¹ Based on the theoretical calculation, the number of free anions in LHCE is more than that in HCE and LCE, which can reduce the energy barrier for anion intercalation and improve stability for CEI formation (Figure 1b). The cointercalation of solvent molecules and anions into graphite can be avoided by the LHCE. Meanwhile, the adequate free anions can induce the formation of an inorganic-rich CEI layer, which protects the graphite structure and prevents continuous anion decomposition. Hence, GDIBs based on the LHCE exhibit an ultralong lifespan of 2400 cycles with a high capacity retention of 85%, significantly outperforming HCE, which achieves 1700 cycles. In addition, the successful operation of pouch-type dual-graphite batteries demonstrates their potential for large-scale application.

RESULTS AND DISCUSSION

The physical and chemical parameters of various electrolytes have been investigated to confirm the practicality of LHCE with the TTE diluent. Permeability is a fundamental prerequisite for the electrolyte to support its rapid diffusion on the electrode surfaces. As shown in Figure S1, a theoretical viscosity of 155 mPa s is attained by the HCE, which is significantly higher than the 36 mPa s of LCE and 14 mPa s of LHCE. More intuitively, the LCE and HCE are not permeated into the polypropylene separator as a cluster in liquid, as shown in Figure S2. In contrast, the LHCE exhibits desirable

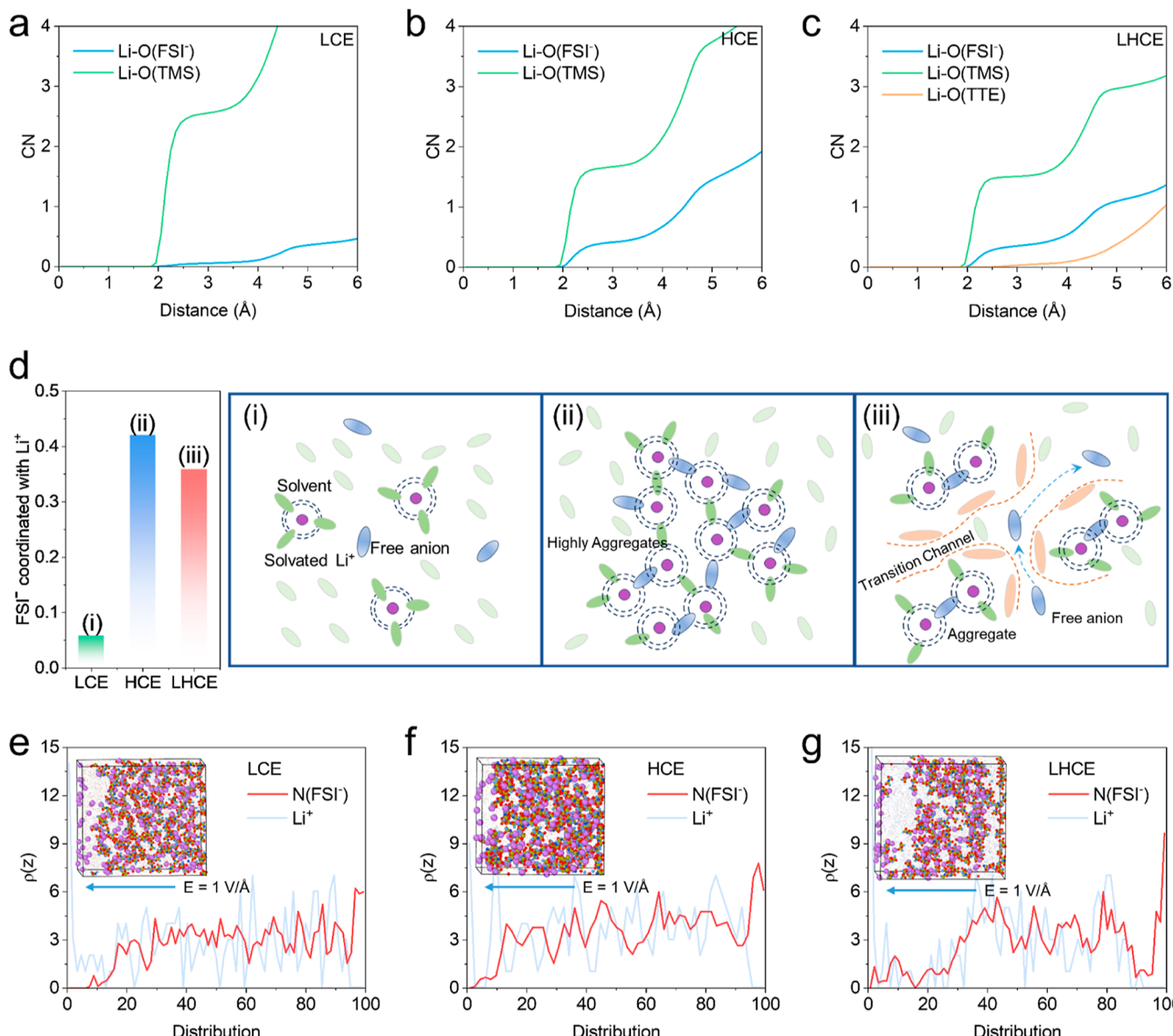


Figure 2. Solvation structure and ion behavior of electrolytes with/without an electric field. (a–c) CN of different electrolytes calculated by MD. (d) Numbers of FSI^- coordinated with Li^+ and a corresponding illustration of electrolyte structures (i–iii). (e–g) Numbers of FSI^- and Li^+ distributed in the electrolyte under an electric field of $1 \text{ V}/\text{\AA}$.

permeability in the separator. We further detected the contact angles of different electrolytes while dropping onto the glass fiber separator, corresponding to 54.9 , 66.8 , and 45.0° of LCE, HCE, and LHCE, respectively (Figure S3). The low viscosity and small contact angle of LHCE may lead to better compatibility and adequate reactivity compared to the LCE and HCE. Besides, as introducing diluent TTE into the LHCE electrolyte, the densities of electrolyte increase from HCE to LHCE. Subsequently, ${}^7\text{Li}$ -nuclear magnetic resonance (nuclear magnetic resonance (NMR)) was carried out to verify the interaction between lithium salt and solvents in various electrolytes (Figure S4). Compared to the pure LiFSI, the ${}^7\text{Li}$ signal of the LCE electrolyte shifts from -1.19 to -1.14 ppm, which can be ascribed to the interaction between Li^+ and solvent.³² With the increasing concentration of LiFSI, the ${}^7\text{Li}$ signal of HCE splits into two signals at -1.17 and -1.08 ppm, corresponding to the interaction between Li^+ with solvent and anions, respectively. It can be inferred that FSI^- anions

participate in Li^+ primary solvation sheath to form cation–anion great aggregates.³¹ The ${}^7\text{Li}$ signal of LHCE has no significant change in number, indicating the weak interaction of Li^+ with anions and more free anions in the electrolyte. Furthermore, Raman spectra were conducted to verify the components of the series electrolytes, pure TTE and TMS (Figure S5). The Raman peaks at 678 , 876 , and 2952 cm^{-1} can be assigned to TMS, while the decreased peak intensity of TMS in HCE and LHCE with the increasing concentrations of LiFSI and TTE can be ascribed to the homogeneous dispersion of salt and diluent in electrolytes. Meanwhile, the Raman peak of free FSI^- anions exhibits a notable blue shift from 725 cm^{-1} in LCE to 745 cm^{-1} in HCE, illustrating that a high concentration of LiFSI may promote more anions to participate in solvation structure. In contrast to HCE, no Raman peak shift was observed after introducing TTE into LHCE, demonstrating that the influence of diluent on

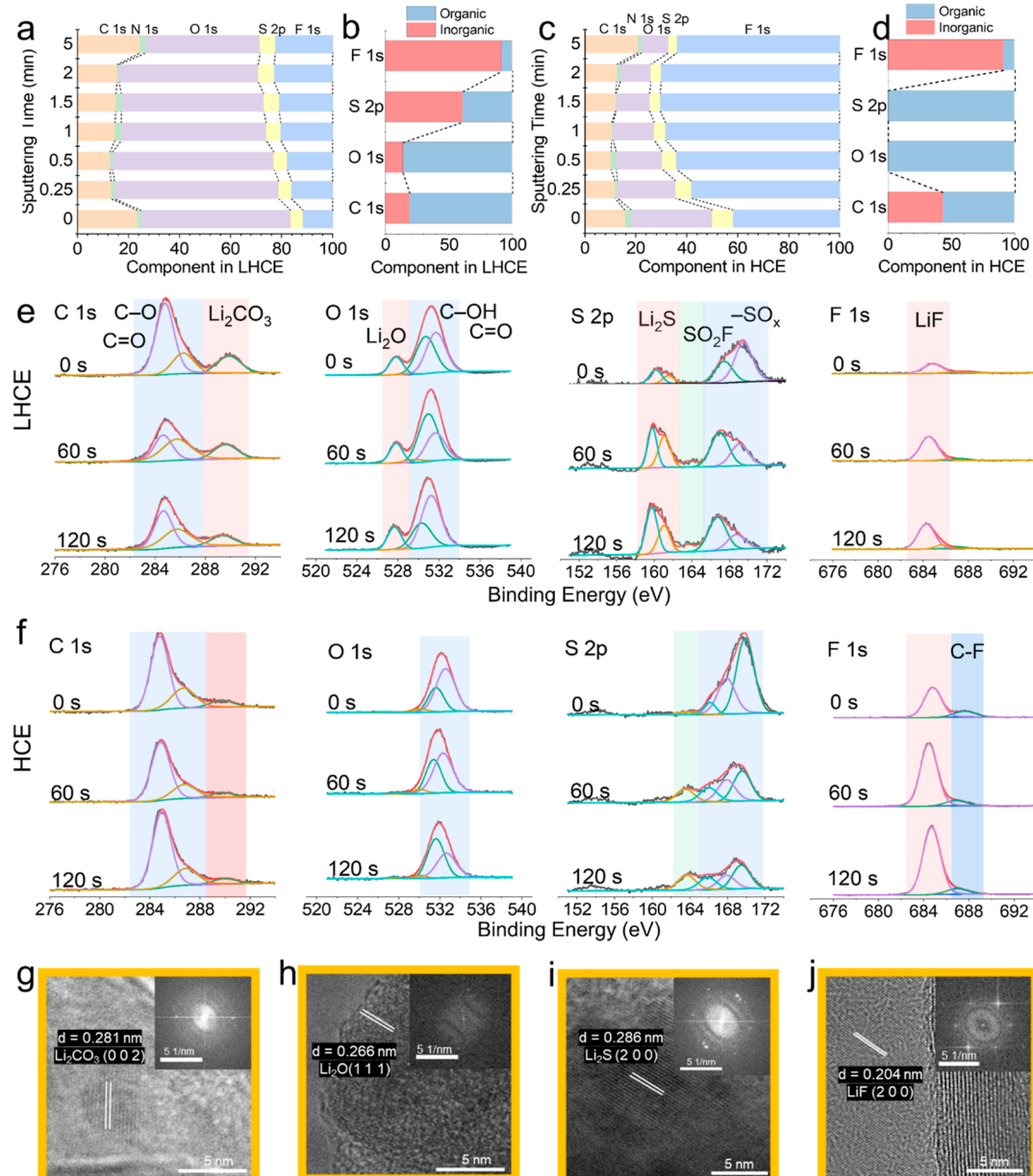


Figure 3. Characterization of the CEI structure on the surface of graphite. (a–d) Components of different elements and compounds for CEI formed on the graphite surface in LHCE and HCE. **(e,f)** In-depth XPS profiles of C 1s, O 1s, S 2p, and F 1s for the CEI formed on the graphite surface in LHCE and HCE. **(g–j)** Cryo-electron microscopy (Cryo-EM) image of graphite cathodes after cycling in LHCE.

solvation structure is negligible and increased free anions are attained.^{33,34}

To investigate the electrochemical stability of various electrolytes, linear sweep voltammetry (LSV) was employed to test the oxidation potential in symmetric stainless steel cells. In Figure S6, the oxidation potentials of various electrolytes are determined as 4.2, 6.2, and 5.6 V for LCE, HCE, and LHCE, respectively, indicating a significant improvement with the increase of concentration. The highest occupied molecular orbital (HOMO) and lowest unoccupied molecular orbital (LUMO) energy of different electrolytes were calculated based on the density functional theory (DFT) method to further illustrate the oxidation resistance of each component (Figure S7). The results indicate that a large amount of anions with a high HOMO value in HCE and LHCE can achieve priority decomposition to form an inorganic-rich CEI layer. Due to the

reduced number of free solvents and the formation of an inorganic-rich CEI layer, HCE and LHCE exhibit broader electrochemical windows compared to that of LCE. Besides, more solvent molecules and anions are involved in the solvation structure for HCE, resulting in a better voltage tolerance.

To better understand the anion environment in different electrolytes, the solvation structures of Li⁺ were investigated by using molecular dynamics (MD) simulation. The varying coordinated numbers (CN) of solvent and diluent molecules in the primary solvation sheaths of Li⁺ are shown in Figure 2a–c (the Li–O sharp peak is detected at 1.95 Å for three electrolytes, as shown in Figure S8). It can be calculated that there is a higher CN of 0.42 for anions in Li⁺ primary solvation sheath of HCE compared to that of 0.08 in LCE, leading to the formation of highly CIPs.³¹ These anions are confined within

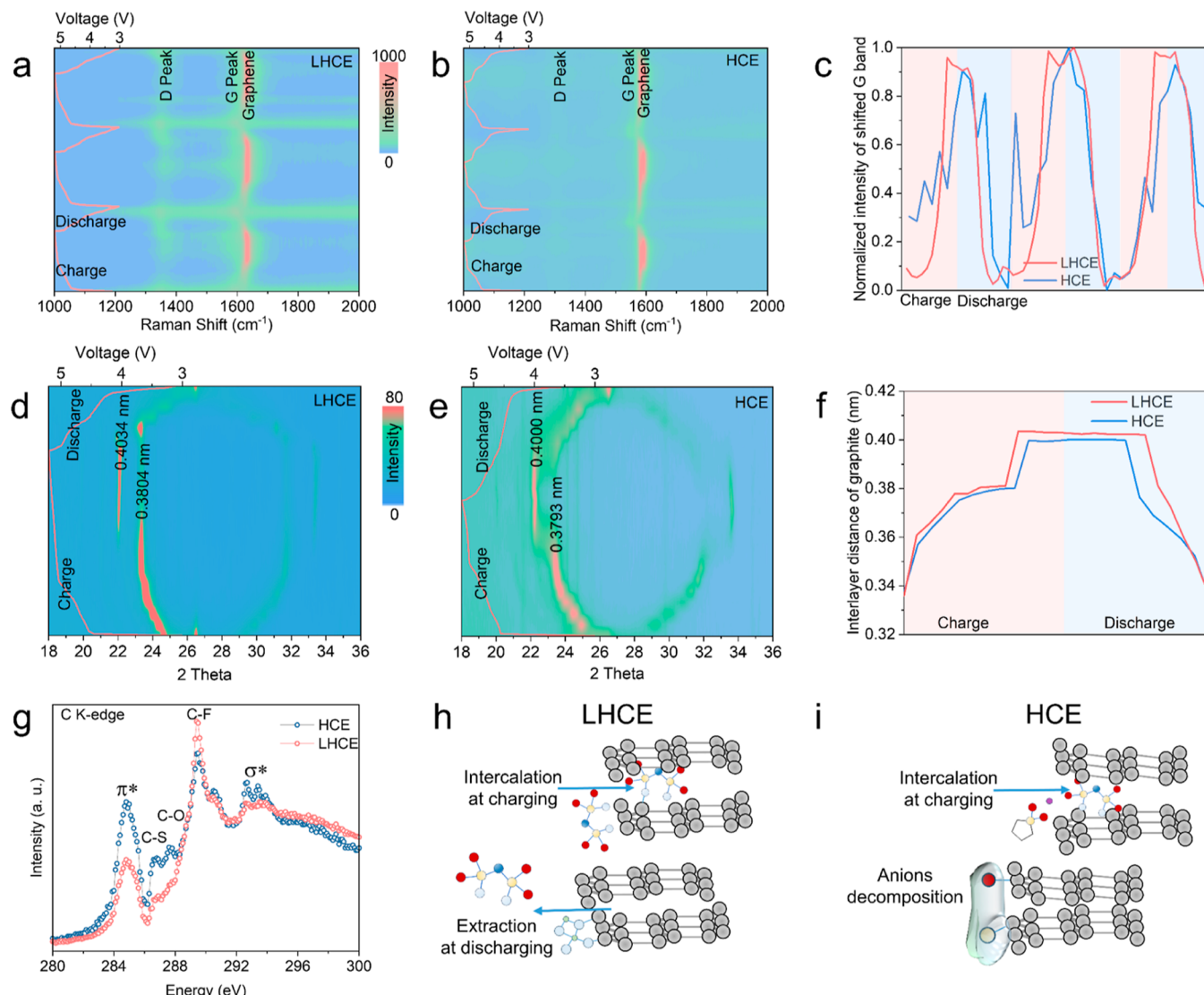


Figure 4. In situ characterizations of graphite in different electrolytes. In situ Raman of cathodic graphite in (a) LHCE and (b) HCE at a current density of 200 mA g^{-1} . (c) Comparison of Raman shifts between LHCE and HCE. In situ X-ray diffraction (XRD) of cathodic graphite in (d) LHCE and (e) HCE at a current density of 200 mA g^{-1} . (f) Comparison of the interlayer distance of graphite between LHCE and HCE. (g) X-ray absorption spectroscopy (XAS) of graphite after five circles of charge/discharge processes at a current density of 200 mA g^{-1} . (The probing depth of soft XAS in the total electron yield mode is around 10 nm). Schematic illustration of the interface of graphite in (h) LHCE and (i) HCE after charge/discharge processes. (Inset Gray = C atoms, Red = O atoms, Yellow = S atoms, Blue = N atoms, White = F atoms, and Green = Li atoms.)

the highly aggregated Li^+ primary solvation sheath, which hinders their independent migration and intercalation. For the solvation structure of Li^+ in LHCE, the addition of TTE diluent creates locally contacted ion pairs with an average CN of 0.36 for anions in the Li^+ primary solvation sheath, while TTE did not penetrate in this process. It can be speculated that anions are released from the highly aggregated Li^+ primary solvation sheath to achieve a free state in the presence of TTE, which may facilitate a highly efficient anion intercalation into the graphite cathode (as depicted in the comparison of intercalation energy barriers in Figure 1).

Figure 2d illustrates the different behaviors of anions under various coordination environments around Li^+ . Although the LCE exhibits a high dissociation ratio of anions in lithium salt with a low concentration, the total amount of anions is still insufficient for dual consumption of intercalation and decomposition. As the concentration of lithium salt increases,

the total number of anions in the HCE and LHCE greatly increases simultaneously. Compared to the HCE, the LHCE possesses smaller coordination energy and more free anions, which is beneficial to rapid transport and stable intercalation of anions.

To further verify the validity of free anion distribution in GDIBs, we analyzed the distribution numbers of anions and cations under an electric field condition. Figure 2e–g shows the distribution numbers (insets are snapshots at 5 ns) of anions and cations in a simulation system with $20 \times 20 \times 20 \text{ nm}$. It can be seen clearly that anions and cations move toward the cathode and anode, respectively. A large number of highly aggregated CIPs with Li^+ in HCE significantly reduces the proportion of free anions migrating to the cathode surface. In contrast, more free anions are released from CIPs and migrate to the cathode surface within the same time frame in LHCE, which facilitates rapid anion intercalation and stable CEI

formation. Hence, the redistribution of anions in LHCE is a benefit to the GDIBs requiring high anionic activity.³⁵

To expound on the anionic effect on interface evolution in different electrolytes, we further investigated the interface composition on the graphite electrode surfaces after five cycles. First, X-ray photoelectron spectroscopy (XPS) with an Ar⁺ sputtering technique was conducted to attain the chemical compositions of CEI layers in different electrolytes. The percentages of C, N, O, S, and F accounting for CEI layers in the LHCE and HCE are shown in Figure 3a,c, respectively. The F content in CEI of HCE is far more than that of LHCE, indicating the continuous decomposition of FSI⁻ and the formation of an F-rich CEI layer in HCE. In contrast, the low F content in CEI of LHCE can be ascribed to the suppressed side reactions by a small amount of coordinated anions and firm interfaces. Furthermore, the proportions of the organic or inorganic components in the interface reaction products of HCE and LHCE are compared to confirm the dominant component for a stable CEI layer (as displayed in Figure 3b,d). In addition to the inorganic compound LiF formed by the decomposition of solvated anions, a considerable amount of inorganic sulfides and oxides are also presented in the LHCE, which results in a multiphase interfacial layer dominated by inorganic substances. It can be inferred that high ionic conductivity and low surface activity can be attained by inorganic-rich interfaces.^{36,37} According to the high-resolution XPS spectra with deep etching (Figure 3e,f and the signals of N 1s are shown in Figure S9), the two deconvoluted signals located at 684.0 and 686.7 eV correspond to the LiF and C—F group, respectively, which shows an increase in organic matter with continuous etching. This result is consistent with a large amount of FSI⁻ consumption in HCE. The C—F component with low conductivity and poor stability is almost undetectable in LHCE, which is replaced by the LiF. The redistribution effect of anions introduced by the diluent TTE undergoes a completely different decomposition process and forms a high-quality CEI layer. Moreover, it can be clearly seen that the organic components of C—OH, C—O, and C=O groups for the C 1s signal around 285.0 eV and the O 1s signal around 531.0 eV are contained in CEI for both electrolytes, while an inorganic Li₂O signal located at 527.1 eV is specifically detected in LHCE. Similarly, the representative organic components of —NH₂, SO₂F, and —SO_x (located at 398.0, 167.0, and 169.0 eV, respectively), which can be observed in both HCE and LHCE. However, the signal of Li₃N located at 396.2 eV and Li₂S located at 160.0 eV are captured only in CEI for LHCE. These inorganic compounds with heterostructures provide fast electric conductivity and good high-voltage tolerance.³³ Fundamentally, the inorganic-rich CEI layer on the graphite electrode was caused by the designed solvation structure with different decomposition paths of FSI⁻ anions.

Additionally, the intuitive compositions of CEI layers in two electrolytes have also been observed using cryo-electron microscopy (cryo-EM) (Figures 3g–j and S10 and S11, and the detailed profiles of gray scale in the vertical direction of the crystal plane are shown in Figure S12). After five cycles, the LHCE exhibits clear lattice fringes of LiF, Li₂S, Li₂O, and Li₂CO₃ in the CEI layers, corresponding to a variety of inorganic compounds with high contents. In contrast, certain amounts of LiF and Li₂CO₃ can be detected on the graphite cathode surface in the HCE after five cycles (as shown in Figure S13). A thick and amorphous CEI layer in HCE may result in slow reaction kinetics and continuous electrolyte

consumption. While the LHCE achieves a stable CEI layer with a dense structure and abundant ionic conductors. These pieces of evidence reveal the redistribution of anions in solvation structure is conducive to the improved interfacial stability of GDIBs.

Figure 4a,b shows the *in situ* Raman spectra of graphite cathodes tested in LHCE and HCE, respectively, under a current density of 200 mA g⁻¹. At the initial state, a doublet peak can be assigned to the D band (1345 cm⁻¹) and G band (1598 cm⁻¹) of natural graphite.^{38–40} For LHCE, a well-defined Raman spectrum with an intensity ratio of periodic fluctuations in D and G bands illustrates the changes in disorder degree caused by the insertion/extraction of anions. During the charging process, the G peak showed a significant blue shift to 1636 cm⁻¹ at a high voltage of 5.2 V, indicating the FSI⁻ anions inserted into interlayers of graphite with an electron transfer (Figure 4a).^{9,41} During the reverse discharging process, the G peak returned to the original position around 1587 cm⁻¹ at a low voltage of 3.0 V, corresponding to the highly reversible extraction of FSI⁻ anions from graphite. In contrast, the red shift of the G peak was also observed in the cycling process in the HCE electrolyte. However, in subsequent cycling, the ratio of the intensity of D and G bands is lower than that in the LHCE electrolyte. The calculated ratios of the shift degree of the G band in different electrolytes are shown in Figure 4c. It can be speculated that the insufficient intercalation of anions constrained by the primary solvation sheath of Li⁺ in HCE, as well as the free anions, plays an important role in reversible intercalation.

Furthermore, to monitor the insertion/extraction behavior of FSI⁻ anions in LHCE and HCE, *in situ* XRD was employed to characterize the changes in lattice parameters of graphite cathodes during the charging and discharging processes. As depicted in Figure 4d, the graphite cathode exhibits a (002) characteristic peak located at $2\theta = 26.5^\circ$, corresponding to the natural graphite. With the insertion of FSI⁻ anions in LHCE, the characteristic peak of natural graphite gradually shifts to the peak at 23.9° when the voltage of GDIB was charged to 5.0 V, indicating that the expanded interlayer spacing of 0.3711 nm was attained by the formation of graphite intercalation compounds (GICs) based on the hierarchical mechanism.⁴² When the voltage of GDIB was further charged to 5.1–5.2 V, the characteristic peaks instantly moved to 22.6 and 20.3°, corresponding to the ultrawide interlayer spacing of 0.4034 and 0.3804 nm, respectively, which can be ascribed to the reconstruction of the stacked graphite structure caused by a large amount of anion insertion (Figure 4f).⁴³ As the GDIB was fully discharged to 3.0 V, the XRD pattern of the graphite cathode gradually returns to the initial position of 26.5°, illustrating good structural reversibility after the release of anions. However, the intensity of the XRD pattern exhibits a significant weakening due to the reduced orderliness and crystallinity. In comparison, the characteristic peak of the graphite cathode in HCE shifted to 22.22° at a cutoff voltage of 5.2 V, leading to an increasing interlayer spacing of 0.400 nm (Figure 4e). There is a gap between the interlayer spacings of graphite cathodes in two electrolytes demonstrating the difference in anion storage capacity (Figure 4f), which can be traced back to free FSI⁻ anions in LHCE with high utilization efficiency of carriers.

Furthermore, XAS was performed on graphite cathodes under the condition of charging to 5.2 V to confirm the dominant factors for high reaction activity and good cycling

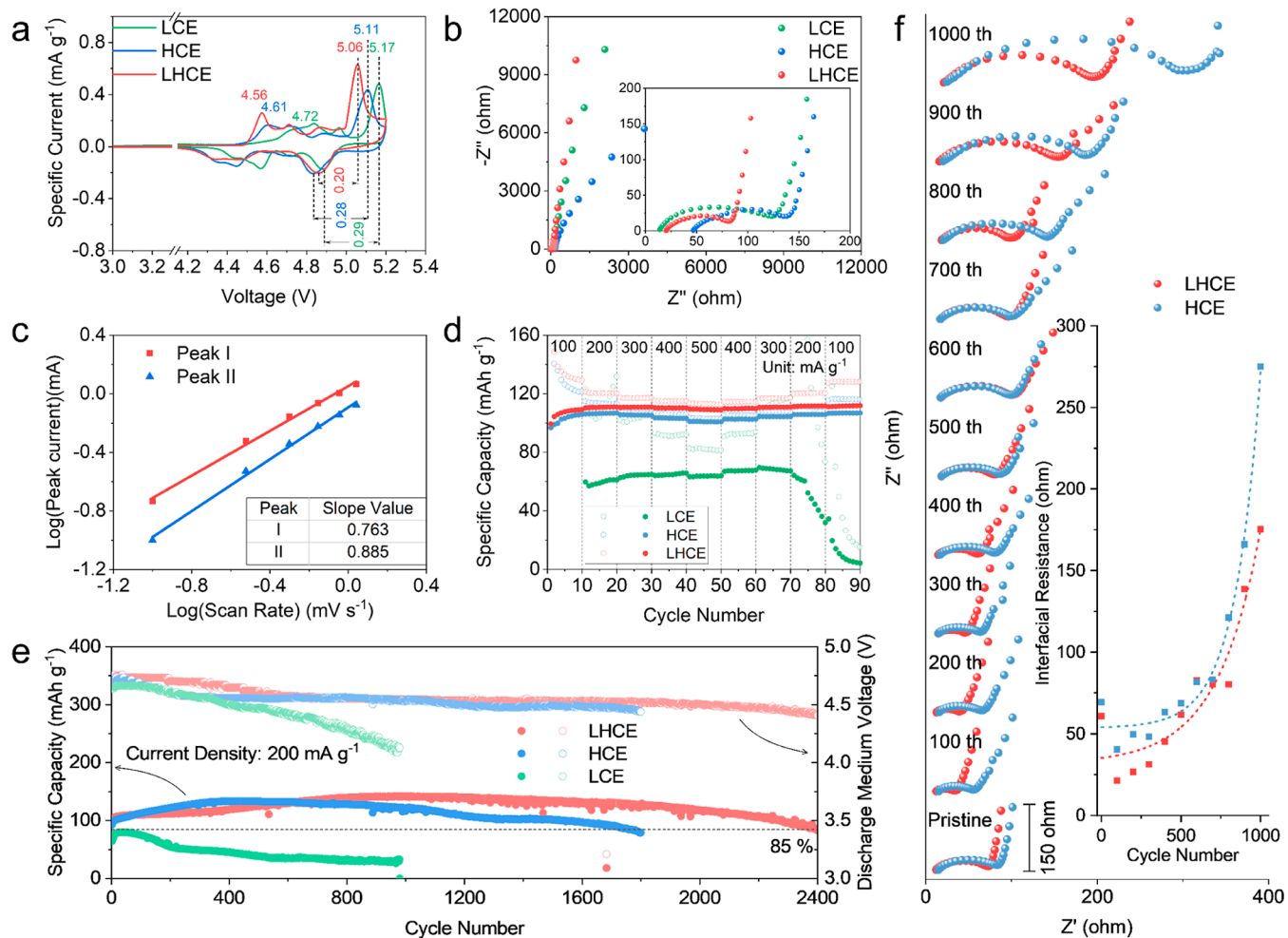


Figure 5. Electrochemical performance of three electrolytes in coin cells. (a) CV of three electrolytes at a scan rate of 0.1 mV s^{-1} between 3 and 5.2 V. (b) EIS of three electrolytes in Li||Graphite cells. (c) Contributions of the pseudocapacity of the cathodic graphite in LHCE. (d) Rate performance of three electrolytes at $100\text{--}500 \text{ mA g}^{-1}$ in Li||Graphite cells. (e) Cycling performance of three electrolytes in Li||Graphite cells. (f) Nyquist plots of EIS in Li||Graphite cells during long cycling in 100 cycles gap. The insert graph is the corresponding values of R_{ct} .

stability in LHCE (Figure 4g). The C K-edge of the fully charged graphite cathodes exhibits two sharp peaks located at 284.9 and 292.6 eV, which are assigned to the transition of C 1s to π^* (sp^2 bond) and σ^* (sp^3 bond).^{44,45} The intensities of π^* and σ^* in LHCE are lower than those in HCE, identifying a thicker CEI layer coated on the graphite cathode in HCE due to the continuous decomposition of anions and a large amount of generated organic matter in the latter (Figure 4h,i).³⁹ Meanwhile, the peaks located at 287.6 and 286.8 eV are attributed to the excitation of C–O and C–S states, originating from solvated anions between graphite layers and decomposition products on graphite surfaces.^{46,47} This result also verifies more anion and solvent consumption in the HCE, as well as the existence of anion–solvent cointercalation with poor reaction activity. According to the high peak intensity of the C–F state in LHCE, it can be inferred that the sufficient free anions are conducive to enhancing the intercalation capacity and reversibility. In brief, the disparity between the contents of C–F and C–S states suggests that free anions not only improve the interface stability but also suppress anion–solvent cointercalation.

To evaluate the electrochemical performance of various electrolytes in GDIBs, we conducted cyclic voltammetry (CV) tests at a scan rate of 0.1 mV s^{-1} using Li || graphite coin cells

with different electrolytes (Figure 5a). The CV curves for all electrolytes consistently displayed three pairs of redox peaks, corresponding to the stepwise formation of GICs.⁴⁸ The onset potentials for FSI⁻ intercalating into the graphite cathode in the LHCE are recorded at 4.56 and 5.06 V, which are lower than those in the HCE (4.61 and 5.11 V) and LCE (4.72 and 5.17 V). This suggests more efficient anion intercalation in the LHCE, likely due to a greater availability of free anions and a lower intercalation energy barrier for intercalation. Furthermore, the peak current intensity of the CV curves in the LHCE is higher than in both the HCE and LCE, indicating a greater number of active carriers being transformed into the graphite cathode to form GICs. Additionally, the lower voltage plateau observed in the LHCE suggests that more anions decomposed at the interface between the electrolyte and cathode during the initial charge, irreversibly forming a stable, inorganic-rich CEI layer. This inorganic-rich CEI layer reduces anion consumption and enhances efficiency during long-term cycling. The polarization voltages between the oxidation and reduction peaks are 0.2 V in the LHCE, compared to 0.28 V in the HCE and 0.29 V in the LCE, further highlighting the superior reaction kinetics in the LHCE. Electrochemical impedance spectroscopy (EIS) was employed to analyze the interfacial kinetics in different electrolytes (Figure 5b). The charge-

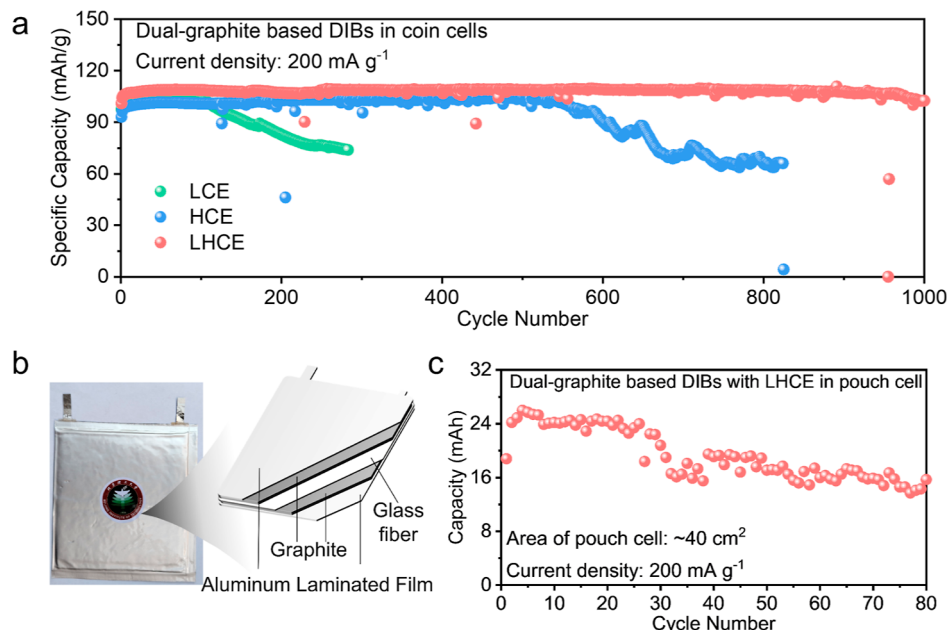


Figure 6. Electrochemical performance of the LHCE-based dual-graphite pouch cell. (a) Cycling performances of different electrolytes in DGDIbs in coin cells. (b) Schematic illustration of DGDIbs in the pouch-type cell. (c) Cycling performance of DGDIbs in the pouch-type cell.

transfer resistance (R_{ct}) in the LHCE was $61.3\ \Omega$, which is smaller than $91.4\ \Omega$ in the HCE and $109.4\ \Omega$ in the LCE, indicating faster charge-transfer dynamics at the interfaces in the LHCE.

Furthermore, CV measurements were performed on Lill graphite cells at various scan rates (Figure S14). The relationship between scan current (i) and scan rate (v) is expressed by the equation: $i = a \times v^b$, where a and b are adjustable coefficients. The b value is determined by the slope of the linear relationship between $\log v$ and $\log i$ (Figure 5c). A b value of 0.5 indicates diffusion-controlled kinetic behavior, while a b value of 1.0 represents a capacitive-controlled kinetic behavior.⁴⁹ The slope values of the LHCE electrolyte were calculated to be 0.763 and 0.885, demonstrating that anion diffusion occurs within the graphite bulk. Additionally, the capacitive and diffusion-dominated contributions of the graphite electrode at a scan rate of 0.1 mV s^{-1} were quantitatively analyzed based on the proportion of k_1v (capacitive) and $k_2v^{1/2}$ (diffusion) at various voltages, using the equation as $i = k_1v + k_2v^{1/2}$.^{50,51} Figure S15 illustrates that the diffusion contribution of the LHCE electrolyte, calculated at a scan rate of 0.1 mV s^{-1} , is 68.1%.

The electrochemical performance under a series of current rates is shown in Figure 5d, with detailed profiles in Figure S16. As the current density increased from 100 to 500 mA g^{-1} , the discharge capacity of GDIBs with LHCE showed no significant decrease. In contrast, the capacity of GDIBs with HCE dropped from 105.8 mA h g^{-1} to 100.7 mA h g^{-1} at 500 mA g^{-1} , while LCE-based cells failed to cycle under 100 mA g^{-1} , delivering only 63 mA h g^{-1} . This highlights the superior rate performance of LHCE compared to that of HCE and LCE in GDIBs. With the long cyclic performance of Li || graphite cells shown in Figure 5e (parallel data shown in Figure S17), the discharge medium voltage of HCE decreased to 4.6 V by the 200th cycle, suggesting structural degradation of the cathodic electrode material, despite an increase in capacity. LCE-based DIBs failed early due to sluggish anion intercalation dynamics

and insufficient anion availability. In contrast, the discharge medium voltage of LHCE remained at 4.7 V after 200 cycles and was maintained at 4.5 V even after 2000 cycles. This indicates faster structural degradation in the graphite electrode with HCE than with LHCE, validating the improved cycling stability of the cathodic electrode in LHCE. This also underscores the impact of anion redistribution on the structural stability of electrode materials in DIBs and their cycling performance. Notably, LHCE electrolytes enabled Li || graphite cells to achieve 85% capacity retention of 83 mA h g^{-1} (cycled between 3.0 and 5.2 V) after 2400 cycles at a current density of 200 mA g^{-1} , compared to HCE-based DIBs, which decayed to 85% after 1800 cycles. The first charge–discharge curves (Figure S18) reveal that the anions in LHCE had a lower initial insertion energy barrier during early insertion stages, with an intercalation voltage plateau of 5.04 V, lower than 5.07 V for HCE and 5.19 V for LCE (consistent with Figure 5a), indicating faster dynamic intercalation. This facilitated easier anion intercalation while maintaining a higher discharge plateau, resulting in a greater discharge energy density.

To further verify the interfacial kinetic performance of LHCE and HCE electrolyte-based DIBs, EIS was performed every 100 cycles over 1000 cycles at a current density of 200 mA g^{-1} (Figure 5f, with detailed electrochemical and EIS data in Figures S19 and S20). The EIS tests revealed an increase in R_{ct} with cycling, yet the R_{ct} of LHCE remained consistently lower than that of HCE, indicating a more stable electrolyte–electrode interphase and more efficient interfacial kinetics throughout long-term cycling. Additionally, the charge and discharge capacities of LHCE after each EIS test were more stable than those of HCE. Besides, we observed the structures of graphite deteriorated after cycling in LCE electrolytes after 10 and 500 cycles due to the LCE electrolyte being very unstable under high voltage conditions (Figure S21a,b). For the HCE electrolyte, as the stability of HCE increases at high voltage, the morphology of graphite is relatively stable after

cycling 10 and 500 cycles in HCE, though many exfoliated fragments appear on the surface (Figure S21c,d). In contrast, the graphite cycled 10 and 500 times in LHCE retains its distinct accordion-like morphology (Figure S21e,f). These pieces of evidence further support the conclusion that anion redistribution enhances the stability and performance of DIBs.

We assembled dual-graphite DIBs (DGDIBs) in both coin-type and pouch-type formats to further evaluate the practicality of LHCE. The graphite electrodes were prelithiated in Lill graphite cells using a commercial electrolyte containing 1 M LiFSI in EC/PC (1:1 in volume ratio) at a constant current density of 200 mA g⁻¹. After prelithiation, the graphite electrodes were washed and used as anodes in the DGDIBs. As shown in Figure 6a, the use of an LHCE effectively addresses issues related to high-voltage stability, interfacial compatibility, and storage kinetics. The DGDIBs with LHCE achieved a high capacity retention of 99% after 1000 cycles at a current density of 200 mA g⁻¹ (based on the graphite cathode). In contrast, DGDIBs using HCE and LCE exhibited significant capacity degradation after 500 and 100 cycles, respectively. Additionally, we assembled pouch-type cells with a laminated structure, as shown in Figure 6b. These pouch-type cells maintained a reversible discharge capacity of around 20 mA h over 80 cycles at a rate of 2 C (1 C = 100 mA g⁻¹), demonstrating significant potential for large-scale applications (Figure 6c).

CONCLUSIONS

In this work, an LHCE was introduced into GDIBs to achieve anion redistribution and interface regulation, resulting in superior reaction activity and cycling stability. It is worth noting that the LHCE not only balances high voltage tolerance and ionic conductivity but also regulates anion decomposition and storage behavior. According to the calculation results, the LHCE shows a large amount of anions released from the Li⁺ primary solvation sheath, leading to fast migration and concentrated distribution of free anions in the electrolyte. These free anions not only enable low intercalation voltage without anion–solvent cointercalation but also form inorganic-rich CEI layers with high ionic conductivity and interfacial compatibility. Meanwhile, the reversible and efficient anion storage behavior can be observed based on the *in situ* measurements. Owing to the suppressed side reactions and enhanced kinetics in LHCE, the GDIBs maintained a high capacity retention of 85% after 2400 cycles, and an outstanding rate performance of 109.2 mA h g⁻¹ can be attained at a current density of 500 mA g⁻¹. In DGDIBs, there is no significant capacity decay during 1000 cycles, illustrating the remarkable compatibility between LHCE and graphite electrodes. Finally, we assembled laminated dual-graphite pouch cells and successfully demonstrated a good application feasibility for large-scale energy storage devices. This work provides a new approach to anion state regulation for designing a high-quality electrolyte, taking into account stability and storage ability.

MATERIALS AND METHODS

Preparation of Materials. LiFSI, TMS, and TTE were purchased as battery-grade from Aladdin Biochemical Technology Co., Ltd. (Shanghai, China). Natural graphite was purchased from Canrd New Energy Technology (Guangdong, China). Chloroform-D¹ was purchased from Bei Jing TongGuang Fine Chemicals Company. Li metal anodes with a 12 mm diameter and 500 μm thickness were purchased from China Energy Lithium. The LCE (LiFSI-8TMS), HCE (LiFSI-3TMS), and LHCE (LiFSI-3TMS-3TTE) were prepared

using TopPette from DLAB Scientific Co., Ltd. as molar ratios in a glovebox by stirring for 24 h at room temperature.

Materials Characterizations. The tests of the contact angle and viscosity were performed on SZ-CAMC32 (Sunzern) and Lovis 2000 M (Anton-Paar). The ⁷Li and ¹H nuclear magnetic resonance (NMR, Bruker AVANCE NEO 400) tests were carried out to demonstrate the electrolyte environment. Chloroform-D¹ was used as a deuterated reagent, and 100 μL of electrolyte was dissolved into 500 μL of Chloroform-D¹ for preparation. Fourier transform infrared spectroscopy was obtained from a Nicolet 6700 spectrometer to analyze the electrolyte structure. Raman spectra tests were conducted to analyze the electrolyte structure by a Thermo Fisher DXR2 microscope spectrometer installed with a HeNe laser and a wavelength of 532 nm.

Field emission scanning electron microscopy (Hitachi S4800, Japan) and XPS (ULVAC-PHI, PHI QUANTERA-II SXM, Japan) were used to observe the morphology and chemical composition of CEI in different electrolyte systems. Cells after the electrochemical test were disassembled in a glovebox with a pure argon atmosphere. Then, the surface of graphite electrodes was washed several times using dimethyl carbonate. Finally, the washed graphite electrodes were dried in an argon atmosphere. After washing, the XPS measurements were carried out with a Thermo ESCALAB 250XI spectrometer using a monochromatic Al K α X-ray source. The cryo-EM was carried out with a 2100 plus transmission electron microscope (TEM, JEOL Ltd.) working at 120 kV with an Elsa cryo-transfer station. *In situ* XRD and *in situ* Raman tests were carried out for materials characterization by using electrochemical cells on D8 ADVANCEDX (Bruker) and DRX2 (Thermo Fisher).

Electrochemical Tests. In order to test the application of three electrolytes in GDIBs, natural graphite as the electrode material was prepared by fully grinding as active materials with conductive carbon black and binder (PVDF) in the ratio of 8:1:1 by mass. The slurry was then coated on carbon-coated aluminum foil and dried at 80 °C for 12 h. After drying, the electrode sheets were cut into small, 11 mm diameter discs and used for battery installation. The thickness of the graphite electrodes is, respectively, 200 and 50 μm for positive and negative electrodes. The areal load of active material on positive and negative electrodes is, respectively, 8 and 3 mg cm⁻².

Coin cells (CR2025, Canrd) were assembled in an argon-filled glovebox (Mikrouna, China). Corrtest electrochemical workstations were used for the impedance measurements with the frequency range of 10–10⁵ Hz and the amplitude of 5 mV. Battery testers (CT-4008T, Neware, China) were used for the galvanostatic measurements at room temperature. The pristine Li foils with the thickness of 500 μm were used in lithium anode GDIBs as the anode, and glass fiber (Whatman) was used as a separator with a diameter of 19 μm.

Density Functional Theory Calculations. All DFT calculation data in this paper were calculated with the Gaussian16 software package and were optimized at the B3LYP level of DFT.⁵² The basis set def2TZVP was selected for all nonmetal atoms. Vibrational frequency analysis was computed to ensure the points that the minimum have no imaginary frequency. All the energetic values reported in this work are Gibbs free energies at 298.15 K. The molecular electrostatic potential (MESP) isosurface was calculated by Multiwfn software, and MEPS maps were visualized by visual molecular dynamics (VMD).⁵³ For HOMO and LUMO calculations, the orbital isosurface value was 0.04.

Molecular Dynamics Simulations. Using the LAMMPS program, we performed molecular dynamics (MD) calculations utilizing the OPLS-AA force field to determine interactions between ions and molecules. Homogeneous electrolyte models were generated with PACKMOL software.⁵⁴ For each isolated electrolyte ion, electronic structure calculations were conducted at the B3LYP/def2TZVP level using Gaussian16 software, followed by the calculation of RESP2-type fitted electrostatic potential charges using Multiwfn software.⁵⁵ To approximate the effects of charge transfer and polarization in the bulk phase, the partial charges of ions were uniformly scaled by 0.8.⁵⁶

Long-range electrostatic interactions were calculated using the particle–particle particle-mesh method with a real-space cutoff

distance of 12 Å, and van der Waals interactions were truncated at 12 Å. The temperature was set to 298 K, and the pressure was set to 1.0 bar, regulated by a Nose–Hoover thermostat and barostat. A fixed electric field of 1 V/Å was applied in the negative Z direction. To avoid unreasonable initial structures, energy minimization was performed for each structure with convergence criteria of 10^{-4} for forces and 10^{-6} for energy, and a time step of 1 fs was used.

First, dynamic equilibration was conducted under zero electric field conditions, with 3 ns of MD simulation in the NPT ensemble followed by 2 ns in the NVT ensemble. Subsequently, under electric field conditions, 8 ns of MD simulation was performed in the NVT ensemble, with the last 2 ns of the trajectory used for the result analysis. Trajectory results and snapshot visualization were analyzed using VMD and OVITO programs, respectively.⁵³

ASSOCIATED CONTENT

SI Supporting Information

The Supporting Information is available free of charge at <https://pubs.acs.org/doi/10.1021/acsnano.Sc03112>.

Viscosity and density of three different electrolytes, contact angle test between electrolytes and glass fiber, NMR test of electrolytes, Raman spectra of components of electrolytes, LSV tests for three different electrolytes, HOMO–LUMO of components of electrolytes, MD calculation of electrolytes, XPS and cryo-EM patterns of graphite after cycling, electrochemical performance of DIBs using different electrolytes, and SEM of graphite after cycling in different electrolytes ([PDF](#))

AUTHOR INFORMATION

Corresponding Authors

Yongxin Huang – Beijing Key Laboratory of Environmental Science and Engineering, School of Material, Science and Engineering, Beijing Institute of Technology, Beijing 100081, China; Shandong Key Laboratory of Advanced Chemical Energy Storage and Intelligent Safety, Advanced Technology Research Institute, Beijing Institute of Technology, Jinan 250300, China; Innovative Research Team in High-Safety Energy Storage System and Smart Microgrids of Guangdong Province, Beijing Institute of Technology (Zhuhai), Zhuhai 519088, China; Email: huangyx@bit.edu.cn

Renjie Chen – Beijing Key Laboratory of Environmental Science and Engineering, School of Material, Science and Engineering, Beijing Institute of Technology, Beijing 100081, China; Shandong Key Laboratory of Advanced Chemical Energy Storage and Intelligent Safety, Advanced Technology Research Institute, Beijing Institute of Technology, Jinan 250300, China; Innovative Research Team in High-Safety Energy Storage System and Smart Microgrids of Guangdong Province, Beijing Institute of Technology (Zhuhai), Zhuhai 519088, China; Collaborative Innovation Center of Electric Vehicles in Beijing, Beijing 100081, China; [orcid.org/0000-0002-7001-2926](#); Email: chenrj@bit.edu.edu

Authors

Xin Hu – Beijing Key Laboratory of Environmental Science and Engineering, School of Material, Science and Engineering, Beijing Institute of Technology, Beijing 100081, China

Wen Sun – Beijing Key Laboratory of Environmental Science and Engineering, School of Material, Science and Engineering, Beijing Institute of Technology, Beijing 100081, China

Anbin Zhou – Beijing Key Laboratory of Advanced Chemical Energy Storage Technologies and Materials, Chemical Defense Institute, Beijing 100191, China

Ziyue Wen – Beijing Key Laboratory of Environmental Science and Engineering, School of Material, Science and Engineering, Beijing Institute of Technology, Beijing 100081, China

Huirong Wang – School of Renewable Energy, Inner Mongolia University of Technology, Ordos 017010, China

Zhengqiang Hu – Beijing Key Laboratory of Environmental Science and Engineering, School of Material, Science and Engineering, Beijing Institute of Technology, Beijing 100081, China

Tianyang Xue – Beijing Key Laboratory of Environmental Science and Engineering, School of Material, Science and Engineering, Beijing Institute of Technology, Beijing 100081, China

Li Li – Beijing Key Laboratory of Environmental Science and Engineering, School of Material, Science and Engineering, Beijing Institute of Technology, Beijing 100081, China; Shandong Key Laboratory of Advanced Chemical Energy Storage and Intelligent Safety, Advanced Technology Research Institute, Beijing Institute of Technology, Jinan 250300, China; Innovative Research Team in High-Safety Energy Storage System and Smart Microgrids of Guangdong Province, Beijing Institute of Technology (Zhuhai), Zhuhai 519088, China; Collaborative Innovation Center of Electric Vehicles in Beijing, Beijing 100081, China; [orcid.org/0000-0001-8859-076X](#)

Feng Wu – Beijing Key Laboratory of Environmental Science and Engineering, School of Material, Science and Engineering, Beijing Institute of Technology, Beijing 100081, China; Shandong Key Laboratory of Advanced Chemical Energy Storage and Intelligent Safety, Advanced Technology Research Institute, Beijing Institute of Technology, Jinan 250300, China; Innovative Research Team in High-Safety Energy Storage System and Smart Microgrids of Guangdong Province, Beijing Institute of Technology (Zhuhai), Zhuhai 519088, China; Collaborative Innovation Center of Electric Vehicles in Beijing, Beijing 100081, China

Complete contact information is available at:

<https://pubs.acs.org/doi/10.1021/acsnano.Sc03112>

Author Contributions

X.H. and Y.H. conceived the idea and designed the project. X.H. and W.S. carried out the experience and electrochemical test. X.H. and Z.W. carried out the in situ XRD, Raman study, and XPS analysis. X.H. and Z.H. performed the theoretical calculation. T.X. and Z.W. performed the schematic drawing. X.H. wrote the original manuscript. L.L., R.C., and F.W. supervised the discussion of the paper. All the authors discussed the results and commented on the manuscript.

Notes

The authors declare no competing financial interest.

ACKNOWLEDGMENTS

We thank Xinghao Yan at Tsinghua University for the test and analysis of Cryo-EM and Shiyanjia Lab (www.shiyanjia.com) for providing invaluable assistance with the XPS tests and analysis. This work was supported by the Joint Funds of the National Natural Science Foundation of China (U2130204), the National Natural Science Foundation of China (52002022), the Young Elite Scientists Sponsorship Program by CAST (YESS20200364), and the Beijing Outstanding Young Scientists Program (BJJWZYJH01201910007023).

REFERENCES

- (1) Tarascon, J.-M.; Armand, M. Issues and challenges facing rechargeable lithium batteries. *Nature* **2001**, *414* (6861), 359–367.
- (2) Winter, M.; Brodd, R. J. What Are Batteries, Fuel Cells, and Supercapacitors? *Chem. Rev.* **2004**, *104* (10), 4245–4270.
- (3) McCullough, F.; Levine, C.; Snelgrove, R. Secondary battery. U.S. Patent 4,830,938 A, 1989.
- (4) Dunn, B.; Kamath, H.; Tarascon, J.-M. Electrical Energy Storage for the Grid: A Battery of Choices. *Science* **2011**, *334* (6058), 928.
- (5) Placke, T.; Heckmann, A.; Schmuck, R.; Meister, P.; Beltrop, K.; Winter, M. Perspective on performance, cost, and technical challenges for practical dual-ion batteries. *Joule* **2018**, *2* (12), 2528–2550.
- (6) Zhou, X.; Liu, Q.; Jiang, C.; Ji, B.; Ji, X.; Tang, Y.; Cheng, H. M. Strategies towards low-cost dual-ion batteries with high performance. *Angew. Chem., Int. Ed.* **2020**, *59* (10), 3802–3832.
- (7) Zhang, L.; Wang, H.; Zhang, X.; Tang, Y. A Review of Emerging Dual-Ion Batteries: Fundamentals and Recent Advances. *Adv. Funct. Mater.* **2021**, *31* (20), 2010958.
- (8) Hofmann, U.; Rüdorff, W. The formation of salts from graphite by strong acids. *Trans. Faraday Soc.* **1938**, *34*, 1017–1021.
- (9) Huang, Z.; Hou, Y.; Wang, T.; Zhao, Y.; Liang, G.; Li, X.; Guo, Y.; Yang, Q.; Chen, Z.; Li, Q.; Ma, L.; Fan, J.; Zhi, C. Manipulating anion intercalation enables a high-voltage aqueous dual ion battery. *Nat. Commun.* **2021**, *12* (1), 3106.
- (10) Kravchyk, K. V.; Bhauriyal, P.; Piveteau, L.; Guntlin, C. P.; Pathak, B.; Kovalenko, M. V. High-energy-density dual-ion battery for stationary storage of electricity using concentrated potassium fluorosulfonylimide. *Nat. Commun.* **2018**, *9* (1), 4469.
- (11) Wang, Y.; Dong, S.; Gao, Y.; Lee, P.-K.; Tian, Y.; Meng, Y.; Hu, X.; Zhao, X.; Li, B.; Zhou, D.; Kang, F. Difluoroester solvent toward fast-rate anion-intercalation lithium metal batteries under extreme conditions. *Nat. Commun.* **2024**, *15* (1), 5408.
- (12) Huang, Z.; Li, X.; Chen, Z.; Li, P.; Ji, X.; Zhi, C. Anion chemistry in energy storage devices. *Nat. Rev. Chem.* **2023**, *7* (9), 616–631.
- (13) Li, W.-H.; Ning, Q.-L.; Xi, X.-T.; Hou, B.-H.; Guo, J.-Z.; Yang, Y.; Chen, B.; Wu, X.-L. Highly Improved Cycling Stability of Anion De-/Intercalation in the Graphite Cathode for Dual-Ion Batteries. *Adv. Mater.* **2019**, *31* (4), 1804766.
- (14) Read, J. A.; Cresce, A. V.; Ervin, M. H.; Xu, K. Dual-graphite chemistry enabled by a high voltage electrolyte. *Energy Environ. Sci.* **2014**, *7* (2), 617–620.
- (15) Rothermel, S.; Meister, P.; Schmuelling, G.; Fromm, O.; Meyer, H.-W.; Nowak, S.; Winter, M.; Placke, T. Dual-graphite cells based on the reversible intercalation of bis(trifluoromethanesulfonyl)imide anions from an ionic liquid electrolyte. *Energy Environ. Sci.* **2014**, *7* (10), 3412–3423.
- (16) Divya, M. L.; Lee, Y.-S.; Aravindan, V. Solvent Co-intercalation: An Emerging Mechanism in Li-, Na-, and K-Ion Capacitors. *ACS Energy Lett.* **2021**, *6* (12), 4228–4244.
- (17) Liu, Q.; Wang, Y.; Yang, X.; Zhou, D.; Wang, X.; Jaumaux, P.; Kang, F.; Li, B.; Ji, X.; Wang, G. Rechargeable anion-shuttle batteries for low-cost energy storage. *Chem.* **2021**, *7* (8), 1993–2021.
- (18) Jiang, H.; Han, X.; Du, X.; Chen, Z.; Lu, C.; Li, X.; Zhang, H.; Zhao, J.; Han, P.; Cui, G. A PF6–Permselective Polymer Electrolyte with Anion Solvation Regulation Enabling Long-Cycle Dual-Ion Battery. *Adv. Mater.* **2022**, *34* (9), 2108665.
- (19) Zhang, H.; Guo, G.; Adenusi, H.; Qin, B.; Li, H.; Passerini, S.; Huang, W. Advances and issues in developing intercalation graphite cathodes for aqueous batteries. *Mater. Today* **2022**, *53*, 162–172.
- (20) Han, X.; Jiang, H.; Mu, P.; Zhang, W.; Zhang, H.; Xu, G.; Chen, Z.; Han, P.; Cui, G. Helmholtz Plane Regulation Empowers PF6– Permselectivity towards High Coulombic Efficiency Dual Ion Battery of 5.5 V. *Angew. Chem., Int. Ed.* **2024**, *64* (1), 202412753.
- (21) Zheng, Y.; Xie, X.; Ueno, H.; Deng, T.; Zheng, W. Manipulating Multivalent Anion Intercalation for High-Energy Aqueous Zn–Graphite Dual-Ion Batteries. *Adv. Energy Mater.* **2024**, *14* (46), 2401914.
- (22) Wu, S.; Gu, X.; Li, Y.; Li, F.; Cheng, Z.; Yao, Q.; Yang, J.; Liu, D.; Li, L.; Dai, P.; Wu, M. Regulating the anion solvation and cathode-electrolyte interphase to improve the reversibility and kinetics of high-voltage dual-ion batteries. *Energy Storage Mater.* **2024**, *72*, 103713.
- (23) Li, G.-X.; Koverga, V.; Nguyen, A.; Kou, R.; Ncube, M.; Jiang, H.; Wang, K.; Liao, M.; Guo, H.; Chen, J.; Dandu, N.; Ngo, A. T.; Wang, D. Enhancing lithium-metal battery longevity through minimized coordinating diluent. *Nat. Energy* **2024**, *9* (7), 817–827.
- (24) Cui, Z.; Jia, Z.; Ruan, D.; Nian, Q.; Fan, J.; Chen, S.; He, Z.; Wang, D.; Jiang, J.; Ma, J.; Ou, X.; Jiao, S.; Wang, Q.; Ren, X. Molecular anchoring of free solvents for high-voltage and high-safety lithium metal batteries. *Nat. Commun.* **2024**, *15* (1), 2033.
- (25) Tong, X.; Ou, X.; Wu, N.; Wang, H.; Li, J.; Tang, Y. High Oxidation Potential ≈6.0 V of Concentrated Electrolyte toward High-Performance Dual-Ion Battery. *Adv. Energy Mater.* **2021**, *11* (25), 2100151.
- (26) Efaw, C. M.; Wu, Q.; Gao, N.; Zhang, Y.; Zhu, H.; Gering, K.; Hurley, M. F.; Xiong, H.; Hu, E.; Cao, X.; Xu, W.; Zhang, J.-G.; Dufek, E. J.; Xiao, J.; Yang, X.-Q.; Liu, J.; Qi, Y.; Li, B. Localized high-concentration electrolytes get more localized through micelle-like structures. *Nat. Mater.* **2023**, *22* (12), 1531–1539.
- (27) Ilic, S.; Lavan, S. N.; Connell, J. G. Anion-derived contact ion pairing as a unifying principle for electrolyte design. *Chem.* **2024**, *10* (10), 2987–3007.
- (28) Gao, P.; Zhang, F.; Wang, X.; Wu, M.; Xiang, Q.; Yang, A.; Sun, Y.; Guo, J.; Huang, Y. Ultrastable Dendrite-Free Potassium Metal Batteries Enabled by Weakly-Solvated Electrolyte. *ACS Nano* **2023**, *17* (20), 20325–20333.
- (29) Liu, L.; Shadik, Z.; Wang, N.; Chen, Y.; Cai, X.; Hu, E.; Zhang, J. Low concentration electrolyte: A new approach for achieving high performance lithium batteries. *eScience* **2024**, *4* (6), 100268.
- (30) Li, M.; Wang, C.; Chen, Z.; Xu, K.; Lu, J. New Concepts in Electrolytes. *Chem. Rev.* **2020**, *120* (14), 6783–6819.
- (31) Ren, X.; Chen, S.; Lee, H.; Mei, D.; Engelhard, M. H.; Burton, S. D.; Zhao, W.; Zheng, J.; Li, Q.; Ding, M. S.; Schroeder, M.; Alvarado, J.; Xu, K.; Meng, Y. S.; Liu, J.; Zhang, J.-G.; Xu, W. Localized High-Concentration Sulfone Electrolytes for High-Efficiency Lithium-Metal Batteries. *Chem.* **2018**, *4* (8), 1877–1892.
- (32) Yao, N.; Chen, X.; Sun, S.-Y.; Gao, Y.-C.; Yu, L.; Gao, Y.-B.; Li, W.-L.; Zhang, Q. Identifying the lithium bond and lithium ionic bond in electrolytes. *Chem.* **2025**, *11*, 102254.
- (33) Qin, L.; Xiao, N.; Zheng, J.; Lei, Y.; Zhai, D.; Wu, Y. Localized High-Concentration Electrolytes Boost Potassium Storage in High-Loading Graphite. *Adv. Energy Mater.* **2019**, *9* (44), 1902618.
- (34) Jiang, L.-L.; Yan, C.; Yao, Y.-X.; Cai, W.; Huang, J.-Q.; Zhang, Q. Inhibiting Solvent Co-Intercalation in a Graphite Anode by a Localized High-Concentration Electrolyte in Fast-Charging Batteries. *Angew. Chem., Int. Ed.* **2021**, *60* (7), 3402–3406.
- (35) Chen, Z.; Tang, Y.; Du, X.; Chen, B.; Lu, G.; Han, X.; Zhang, Y.; Yang, W.; Han, P.; Zhao, J.; Cui, G. Anion Solvation Reconfiguration Enables High-Voltage Carbonate Electrolytes for Stable Zn/Graphite Cells. *Angew. Chem., Int. Ed.* **2020**, *59* (48), 21769–21777.
- (36) Wan, H.; Xu, J.; Wang, C. Designing electrolytes and interphases for high-energy lithium batteries. *Nat. Rev. Chem.* **2024**, *8* (1), 30–44.
- (37) Yang, J.; Liu, X.; Wang, Y.; Zhou, X.; Weng, L.; Liu, Y.; Ren, Y.; Zhao, C.; Dahbi, M.; Alami, J.; Ei-Hady, D. A.; Xu, G.-L.; Amine, K.; Shao, M. Electrolytes Polymerization-Induced Cathode-Electrolyte-Interphase for High Voltage Lithium-Ion Batteries. *Adv. Energy Mater.* **2021**, *11* (39), 2101956.
- (38) Zhao, S.; Li, G.; Zhang, B.; Zhang, S.; Liu, Y.; Zhou, J.; Luo, M.; Guo, S. Highly-Solvating Electrolyte Enables Mechanically Stable and Inorganic-Rich Cathode Electrolyte Interphase for High-Performing Potassium-Ion Batteries. *Adv. Mater.* **2024**, *36* (32), 2405184.

- (39) Ferrari, A. C. Raman spectroscopy of graphene and graphite: Disorder, electron–phonon coupling, doping and nonadiabatic effects. *Solid State Commun.* **2007**, *143* (1), 47–57.
- (40) Lucchese, M. M.; Stavale, F.; Ferreira, E. H. M.; Vilani, C.; Moutinho, M. V. O.; Capaz, R. B.; Achete, C. A.; Jorio, A. Quantifying ion-induced defects and Raman relaxation length in graphene. *Carbon* **2010**, *48* (5), 1592–1597.
- (41) Xiang, L.; Ou, X.; Wang, X.; Zhou, Z.; Li, X.; Tang, Y. Highly Concentrated Electrolyte towards Enhanced Energy Density and Cycling Life of Dual-Ion Battery. *Angew. Chem., Int. Ed.* **2020**, *59* (41), 17924–17930.
- (42) Oka, H.; Makimura, Y.; Uyama, T.; Nonaka, T.; Kondo, Y.; Okuda, C. Changes in the stage structure of Li-intercalated graphite electrode at elevated temperatures. *J. Power Sources* **2021**, *482*, 228926.
- (43) Andersen, H. L.; Djuandhi, L.; Mittal, U.; Sharma, N. Strategies for the Analysis of Graphite Electrode Function. *Adv. Energy Mater.* **2021**, *11* (48), 2102693.
- (44) Xia, D.; Jeong, H.; Hou, D.; Tao, L.; Li, T.; Knight, K.; Hu, A.; Kamphaus, E. P.; Nordlund, D.; Sainio, S.; Liu, Y.; Morris, J. R.; Xu, W.; Huang, H.; Li, L.; Xiong, H.; Cheng, L.; Lin, F. Self-terminating, heterogeneous solid–electrolyte interphase enables reversible Li–ether cointercalation in graphite anodes. *Proc. Natl. Acad. Sci. U.S.A.* **2024**, *121* (5), No. e2313096121.
- (45) Wang, D.-Y.; Wei, C.-Y.; Lin, M.-C.; Pan, C.-J.; Chou, H.-L.; Chen, H.-A.; Gong, M.; Wu, Y.; Yuan, C.; Angell, M.; Hsieh, Y.-J.; Chen, Y.-H.; Wen, C.-Y.; Chen, C.-W.; Hwang, B.-J.; Chen, C.-C.; Dai, H. Advanced rechargeable aluminium ion battery with a high-quality natural graphite cathode. *Nat. Commun.* **2017**, *8* (1), 14283.
- (46) Ji, L.; Rao, M.; Zheng, H.; Zhang, L.; Li, Y.; Duan, W.; Guo, J.; Cairns, E. J.; Zhang, Y. Graphene Oxide as a Sulfur Immobilizer in High Performance Lithium/Sulfur Cells. *J. Am. Chem. Soc.* **2011**, *133* (46), 18522–18525.
- (47) Liang, Y.; Li, Y.; Wang, H.; Zhou, J.; Wang, J.; Regier, T.; Dai, H. Co₃O₄ nanocrystals on graphene as a synergistic catalyst for oxygen reduction reaction. *Nat. Mater.* **2011**, *10* (10), 780–786.
- (48) Beltrop, K.; Madrid Madrid, J. C.; Meister, P.; Heckmann, A.; Winter, M.; Akbay, T.; Ishihara, T.; Placke, T. Experimental and computational studies of electrochemical anion intercalation into graphite from target-oriented designed borate-based ionic liquid electrolytes. *J. Power Sources* **2020**, *469*, 228397.
- (49) Choi, C.; Ashby, D. S.; Butts, D. M.; DeBlock, R. H.; Wei, Q.; Lau, J.; Dunn, B. Achieving high energy density and high power density with pseudocapacitive materials. *Nat. Rev. Mater.* **2020**, *5* (1), 5–19.
- (50) Liu, T. C.; Pell, W. G.; Conway, B. E.; Roberson, S. L. Behavior of Molybdenum Nitrides as Materials for Electrochemical Capacitors: Comparison with Ruthenium Oxide. *J. Electrochem. Soc.* **1998**, *145* (6), 1882.
- (51) Wang, J.; Polleux, J.; Lim, J.; Dunn, B. Pseudocapacitive Contributions to Electrochemical Energy Storage in TiO₂ (Anatase) Nanoparticles. *J. Phys. Chem. C* **2007**, *111* (40), 14925–14931.
- (52) Frisch, M. J.; Trucks, G. W.; Schlegel, H. B.; Scuseria, G. E.; Robb, M. A.; Cheeseman, J. R.; Scalmani, G.; Barone, V.; Petersson, G. A.; Nakatsuji, H.; Li, X.; Caricato, M.; Marenich, A. V.; Bloino, J.; Janesko, B. G.; Gomperts, R.; Mennucci, B.; Hratchian, H. P.; Ortiz, J. V.; Izmaylov, A. F.; Sonnenberg, J. L.; Williams-Young, D.; Ding, F.; Lipparini, F.; Egidi, F.; Goings, J.; Peng, B.; Petrone, A.; Henderson, T.; Ranasinghe, D.; Zakrzewski, V. G.; Gao, J.; Rega, N.; Zheng, G.; Liang, W.; Hada, M.; Ehara, M.; Toyota, K.; Fukuda, R.; Hasegawa, J.; Ishida, M.; Nakajima, T.; Honda, Y.; Kitao, O.; Nakai, H.; Vreven, T.; Throssell, K.; Montgomery, J. A., Jr.; Peralta, J. E.; Ogliaro, F.; Bearpark, M. J.; Heyd, J. J.; Br, E. N.; Kudin, K. N.; Staroverov, V. N.; Keith, T. A.; Kobayashi, R.; Normand, J.; Raghavachari, K.; Rendell, A. P.; Burant, J. C.; Iyengar, S. S.; Tomasi, J.; Cossi, M.; Millam, J. M.; Klene, M.; Adamo, C.; Cammi, R.; Ochterski, J. W.; Martin, R. L.; Morokuma, K.; Farkas, O.; Foresman, J. B.; Fox, D. J. *Gaussian*, *16*, Revision, C.01.; Gaussian, Inc.: Wallingford, CT, 2016.
- (53) Humphrey, W.; Dalke, A.; Schulter, K. VMD: Visual molecular dynamics. *J. Mol. Graphics* **1996**, *14* (1), 33–38.
- (54) Martínez, L.; Andrade, R.; Birgin, E. G.; Martínez, J. M. PACKMOL: A package for building initial configurations for molecular dynamics simulations. *J. Comput. Chem.* **2009**, *30* (13), 2157–2164.
- (55) Lu, T.; Chen, F. Multiwfn: A multifunctional wavefunction analyzer. *J. Comput. Chem.* **2012**, *33* (5), 580–592.
- (56) Zhao, Y.; Hu, Z.; Zhao, Z.; Chen, X.; Zhang, S.; Gao, J.; Luo, J. Strong Solvent and Dual Lithium Salts Enable Fast-Charging Lithium-Ion Batteries Operating from –78 to 60 °C. *J. Am. Chem. Soc.* **2023**, *145* (40), 22184–22193.